Time-domain and lock-in rate-window photocarrier radiometric measurements of recombination processes in silicon

Andreas Mandelis[a)]
Institut für Experimentalphysik III, Festkörperspektroskopie, Ruhr Universität Bochum, D-44780 Bochum, Germany and Center for Advanced Diffusion-Wave Technologies (CADIFT), Department of Mechanical and Industrial Engineering, University of Toronto, Toronto M5S 3G8, Canada

Micha Pawlak
Institut für Experimentalphysik III, Festkörperspektroskopie, Ruhr Universität Bochum, D-44780 Bochum, Germany

Chinhua Wang
Center for Advanced Diffusion-Wave Technologies (CADIFT), Department of Mechanical and Industrial Engineering, University of Toronto, Toronto M5S 3G8, Canada

Isabel Delgadillo-Holtfort and Josef Pelzl
Institut für Experimentalphysik III, Festkörperspektroskopie, Ruhr Universität Bochum, D-44780 Bochum, Germany

(Received 11 April 2005; accepted 7 November 2005; published online 27 December 2005)

Time-domain and lock-in rate-window photocarrier radiometry (PCR) configurations are introduced both experimentally and theoretically to investigate the responses of *p*- and *n*-type Si wafers under a repetition-period-scanned square-wave-modulated super-band-gap laser beam which produces free excess photocarriers. The complete asymmetric time-domain carrier diffusion and recombination boundary-value problem with different front- and back-surface recombination velocities was solved in terms of the full spectrum of spatial eigenmodes and used to fit the time-domain data. The accurate measurement of the photocarrier transport properties (bulk lifetime, surface recombination velocities, and ambipolar diffusivity) was found to require the linear superposition of all the effective decay lifetimes associated with the eigenmode spectrum. The effects of the infinite prior pulse train to the current photocarrier radiometric response wave form were quantified and were found to be very important for certain ranges of transport parameters, pulse durations, and repetition periods. The time-domain formalism was further used to develop a theory for lock-in rate-window photocarrier radiometry. The application of the theory to the experimental results shows that they retain the time-domain character of the photocarrier generation and recombination processes, with data quality and signal-to-noise ratio superior to coaddition-averaged transients, especially in the case of samples exhibiting very low time-domain PCR signals. © *2005 American Institute of Physics*. [DOI: 10.1063/1.2148631]

I. INTRODUCTION

Laser pump-probe time-domain photoexcitation techniques have been used for some time to monitor recombination processes in semiconductors in a noncontact and nondestructive manner, thus eliminating the need for electrode attachment required by conventional electrical methods.[1–4] These methods combine super-band-gap and sub-band-gap laser wavelengths and measure changes (increases) in the infrared optical-absorption coefficient of a semiconductor due to the excess photoexcited free carriers above the equilibrium density created by the super-band-gap pump-laser pulse. These changes are monitored by the time-dependent transmission transient of the collinearly or crossaligned transmitted or reflected sub-band-gap laser beam. Typically, such two-laser methodologies have been used to measure the surface recombination velocities and bulk recombination lifetimes of *n*- and *p*-type Si wafers.[4,5] Inherent limitations of these methods arise from the fixed wavelength of the probe-laser beam which cannot be properly tuned to optimize the effects of free photoexcited carrier infrared absorption of the transmitted probe. Furthermore, significant additive noise introduced by the incoherent overlap of the two laser beams, each with its own noise characteristics, is exacerbated by the restricted interaction volume between the two beams. Two-laser modeling complexities stem from the spatial profiles of the two beams and require three-dimensional treatments. Last, but not least, two-laser methodologies suffer from the frequently significant background signal level of the unattenuated transmitted probe beam, which tends to mask minute changes in infrared absorption associated with small excess photocarrier density under low-injection conditions. As a result, these techniques exhibit dynamic range limitations for the electronic transport parameters they measure. Furthermore, unlike contacting electrical probe techniques, all optical photocarrier excitation methods to date operate in the high-injection regime. This is possibly a detrimental effect, as recombination parameters under high injection depend on injection level[6,7] and may not be representative of

[a)]Electronic mail: mandelis@mie.utoronto.ca

the true values of the transport properties of the semiconductor while nonlinear diffusion may become a significant carrier decay pathway.[8] A photothermal beam-deflection variant of the optical pump-probe technique has been introduced by Skumanich *et al.*[9] This method is a significant improvement as it yields directional changes of the infrared probe beam as a function of the excess photocarrier density and thermal-wave processes, thus suppressing the signal base line and increasing the dynamic range of the measurement due to its harmonic laser intensity modulation and lock-in detection character. Physically, the technique hinges on superposed thermally and electronically induced changes in the local index of refraction of the semiconductor and yields signals proportional to the gradient of the depth profile of the excess photocarriers. Nevertheless, the other characteristics of the two-beam methodology remain.

Although, in principle, both harmonic and transient photoexcitation and detection lead to equivalent measurements of the electronic recombination transport parameters, an important advantage of time-domain detection of the excess photocarrier density evolution and other diffusion-driven phenomena is the ability to enhance or diminish the importance of the contribution to the signal of particular transport parameters by time gating and thus minimizing the well-known ambiguity[10] due to the nonunique nature of solutions to the carrier harmonic diffusion-wave problem.[11,12] This time weighing cannot be done in frequency-domain measurements: its Fourier-transform nature requires an infinite time span contributing to a single frequency content of the carrier-diffusion-wave field.[13] To take advantage of these parameter-selectivity aspects of time-domain diffusion while minimizing the effects of noise and interacting pump-probe laser beams, Mandelis *et al.*[14] and Chen *et al.*[15] introduced the lock-in rate-window method to the excess photocarrier-diffusion problem using laser infrared photothermal radiometry (PTR) as the detection method. In doing so they succeeded in separating thermal wave from photocarrier contributions to the signals through time gating.[14] They measured bulk recombination lifetimes using a simplified single-laser-pulse diffusion model which did not allow for the effects of the infinite pulse train or for the accurate determination of the other transport parameters (surface recombination velocities and ambipolar carrier diffusivity) in a photoexcited semiconductor.

In this report, lock-in rate-window detection of carrier-diffusion waves is revisited both experimentally and theoretically using as the detection principle the evolution of photothermal radiometry into the recently introduced laser photocarrier radiometry (PCR) of semiconductors,[16] a form of room-temperature photoluminescence (PL). Unlike modulated PTR, PCR has the advantage over photothermal techniques of spectrally filtering out all thermal blackbody (Planck) emissions from photoexcited semiconductors thus yielding higher sensitivity to purely electronic transport and recombination phenomena and greatly simplifying the task of signal interpretation solely in terms of electronic carrier-diffusive transport. Furthermore, it yields superior signal-to-noise ratio (SNR) as the infrared InGaAs detectors typically used in PCR are not thermal noise limited, unlike mid-IR detectors such as HgCdTe. PCR uses a narrow spectral window to detect near-band-gap infrared emissions originating in the radiatively recombining free-carrier-density wave. In Si, PCR originates in the form of infrared photon generation, induced by low-quantum-yield band-to-defect or impurity-state radiative recombination at room temperature[17] and above. This nonequilibrium radiative emission is a manifestation of Kirchhoff's detailed balance,[16,18] and it is considered to be a type of photoluminescent process. Nevertheless, conventional room-temperature PL in Si has rarely been reported and it invariably involves band-to-band bipolar recombination via photoexcited electron and hole excess densities in the high-injection regime ($>10^{16}$ cm^{-3}). Room-temperature PL is generally a nonlinear two-body process of electron-hole band-to-band recombination at high photoexcitation densities. It is fast (~ 2.9 μs decay time[19]) and thus requires considerably higher frequencies (100 kHz–10 MHz) than PCR.[16] King and Hall have performed spectroscopic studies of near-band-edge PL emissions from silicon[17] at 30, 130, and 300 K in the spectral region between 1000 and 1700 nm, which coincides with the InGaAs spectral bandwidth. They used a liquid-nitrogen-cooled InAs detector and reported two broadened peaks at 300 K: one peak approximately centered at 1120 nm very near the band edge, presumably due to band-to-band electron-hole recombination, and a more prominent peak centered at ca. 1700 nm which was identified as the well-known P line[20] and was associated with radiative emissions from recombination at an unidentified defect complex in which oxygen plays a central role. They also measured the external quantum efficiency of the PL process(es) involved in the PL emission and found it to be ca. 2.5×10^{-5} at 300 K. Although it is not fully established that PCR probes the kinetics of this particular recombination process within the $0.7-1.7$ μm bandwidth of the InGaAs detector, using this method it was shown[16] that very deep subsurface defects, as far away as the back surface of a Si wafer, can compromise the electronic transport in the very-near upper surface region where devices are fabricated.

II. MATERIALS AND EXPERIMENTAL SETUP

Lock-in rate-window diffusion-wave techniques can be implemented using a repetitive excitation pulse of duration τ_p and either scanning the pulse duration, while keeping the repetition rate (period T_0) fixed, or scanning the repetition period while keeping τ_p fixed.[14,15,21] In this work the former operating mode was chosen for reasons of experimental convenience. A 4-in. (100)-oriented $5-10$ Ω cm, $500-\mu$m-thick, p-type Si wafer oxidized with a gate oxide of ca. 1000 Å and a 4-in. (100)-oriented n-type Si wafer (unknown resistivity and growth conditions) with ca. 5000 Å oxide were used. Both wafers were industrial samples with polished front sides and matte (rough) backsides. The experimental PCR system configuration is shown in Fig. 1. Oxidized wafers are important for these studies as they present stable $Si-SiO_2$ interfaces to the laser beam, thus avoiding PCR signal drift. The modulated laser source was an Ar-ion laser (514 nm; 1.89 mm beam radius). The beam radius was characterized using a pinhole-on-detector system scanned across

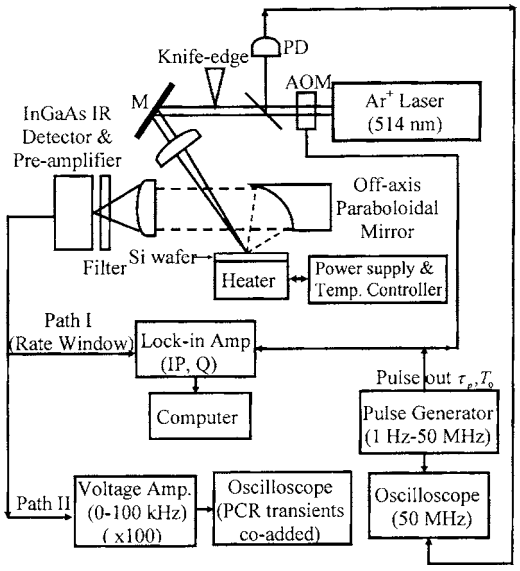

FIG. 1. Lock-in rate-window PCR experimental configuration for laser-pulse generation with fixed τ_p and variable T_0.

the beam profile with a neutral density filter to avoid photodetector saturation. The IR detector was a switchable-gain InGaAs element (ThorLabs model PDA400), 1 mm in diameter, with spectral response in the 800–1750 nm range, peak response at 1550 nm, and frequency bandwidth from dc to 10 MHz. The preamplifier was incorporated into the detector housing, a design which delivered optimal signal-to-noise ratio expressed as a noise-equivalent power (NEP) figure of $(2.9-8.2)\times 10^{-12}$ W/$\sqrt{\text{Hz}}$. The detector was outfitted with a specialty long-pass optical filter from Spectrogon (LP =1000 nm) featuring steep cuton (5% at 1010 nm and 78% at 1060 nm) and transmission range of 1042–2198 nm. The cut-on quality of the filter is crucial in PCR as it must block any synchronous pump radiation leakage from reaching the highly sensitive detector. Short-wavelength filtering of optical density 5 or 6 is usually required. The samples were placed on an aluminum backing which acted as a mechanical support and signal amplifier by redirecting the backward emitted IR photons forward toward the detector.[16] Typical modulated power was 350–400 mW. Taking into account the reflectivity of Si at 514 nm at normal incidence ($R=0.38$) and the laser beam radius $r=1890$ μm, the effective maximum photon flux at 350 mW was $F_{p\,\max}=1.103\times 10^{19}$ photons/cm^2 s.

TABLE II. Fitted transport parameters of *p*-Si sample at various temperatures.

T (°C)	Front-surface recombination velocity (S_1)(cm/s)	Rear-surface recombination velocity (S_2)(cm/s)	Carrier-diffusion coefficient (D_p)(cm^2/s)	Bulk carrier lifetime $(\tau)(\mu s)$
23	14.1	1.1×10^4	18.3	151.3
78	13.2	9.6×10^3	16.3	164.5
176	11.9	9.9×10^3	14.4	173.0
256	11.2	9.5×10^3	12.9	177.5

Assuming unity optical-to-electron-hole-pair photon energy conversion efficiency, the maximum free-carrier flux in our experiments was

$$F_e=\frac{3.43\times 10^{17}}{\pi(r+\sqrt{D_n\tau_n})^2}=1.13\times 10^{18}\ \text{electrons/cm}^2\,\text{s},$$

which corresponds to a free-minority electron flux in our *p*-type Si wafer. This sample exhibited the highest PCR signals. Here the dc minority diffusion length $L_n=(D_n\tau_n)^{1/2}=0.067$ cm for typical values of $D_n\sim 30$ cm^2/s and $\tau_n\sim 150$ μs according to our results for *p*-Si, Tables I and II. Therefore, the experiments were conducted in the high-injection regime,[7] typical of optical injection techniques. Nevertheless, in order to ascertain the linearity of the PCR signal with laser power, which, in turn, validates the linear theory presented in Sec. IV, Fig. 2 shows the dependence of the PCR amplitude on incident laser power. It is seen that the PCR signal amplitude increases with $I^{0.99}$ in the range of powers used in this work (20–400 mW), i.e., in the linear regime, despite the high-injection condition. The PCR phase is also independent of power in that linear range, as expected and predicted in the linear PCR theory.[16] Preliminary measurements of PCR transients and lock-in rate-window responses at several incident powers in the 300–400 mW range did not yield any measurable differences in the values of the material transport properties, thus validating the independence of these properties from intensity and the absence of nonlinear effects.

The samples were placed on a heater powered by a homemade power supply and capable of reaching temperatures up to 300 °C. The emitted infrared radiation from the samples was collected and collimated by an off-axis paraboloidal mirror (Oriel model 45357) and was focused on the

TABLE I. Comparison of the fitted transport parameters of *p*-Si sample and *n*-Si sample at room temperature using transient, Eq. (22), and rate window, Eqs. (25) and (27), methods.

	Front-surface recombination velocity (S_1)(cm/s)	Rear-surface recombination velocity (S_2)(cm/s)	Carrier-diffusion coefficient (D_p, D_n) ×(cm^2/s)	Bulk carrier lifetime $(\tau)(\mu s)$
Transient (*n* type)	278.0	3.1×10^4	D_p:16.7 (10.0–15.9)[a]	13.3 (1 μs–1 ms)[a]
Rate window (*n* type)	264.2	2.7×10^4	D_p:18.3 (10.0–15.9)[a]	12.4 (1 μs–1 ms)[a]
Transient (*p* type)	13.7	1.2×10^4	D_n:25.4 (18.3–37)[a]	154.8 (40 μs–10 ms)[a]
Rate window (*p* type)	14.1	1.1×10^4	D_n:25.9 (18.3–37)[a]	151.3 (40 μs–10 ms)[a]

[a]Reference 29.

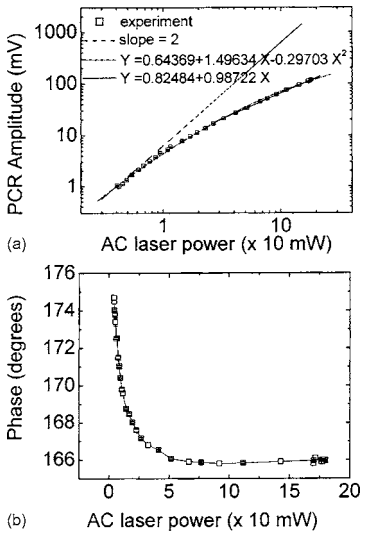

FIG. 2. Laser power dependence of (a) PCR amplitude and (b) phase of a *p*-type Si wafer used in time-domain and rate-window experiments under harmonically modulated conditions at 10 kHz. The amplitude shows best-fit power laws to the data, including a linear fit ($\sim I^{0.99}$) in the range of 20–400 mW. The phase is also independent of power in that range.

detector using simple lens optics. The laser beam was modulated acousto-optically using a square waveform from a pulse generator (Fluke & Philips model PM 5715; 1 Hz–50 MHz bandwidth). The waveform was fed directly to the acousto-optic modulator (AOM) to produce the desired optical excitation waveform incident on the sample. For rate-window measurements this waveform was also split into a second branch which was fed to the lock-in amplifier (LIA, SRS model 830) reference port acting as reference signal. For PCR time-domain waveforms, a 50% duty cycle square wave was generated and the resulting PCR waveform was displayed on a transient oscilloscope ("path II") bypassing the LIA stage and thus requiring additional amplification by a homemade voltage amplifier (dc-100 kHz bandwidth; 100 $\times$amplification), followed by computer display of the average value of several hundreds of coadded PCR transient traces, depending on the noise level associated with each sample and measurement. For rate-window measurements, the square pulse waveform duration τ_ρ of the voltage output

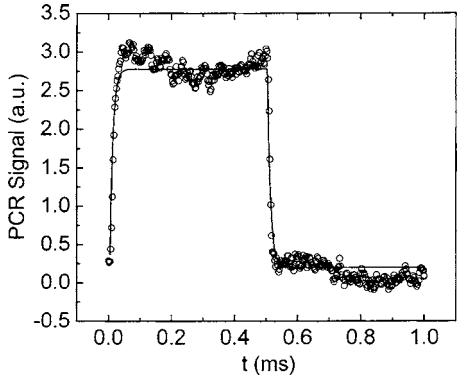

FIG. 3. Room-temperature experimental and best-fitted PCR transient results for *n*-Si sample using transient PCR theory with an infinite pulse train, Eq. (22). Wafer thickness $x_0=502$ μm, $\tau_p=0.5$ ms, and $T_0=1$ ms. Other constants are $\lambda=500$ nm (corresponding to $\alpha\approx 10^4$ cm^{-1}) and $R_1\sim R_2=0.5$. Solid line: theoretical fit; circles: experimental data.

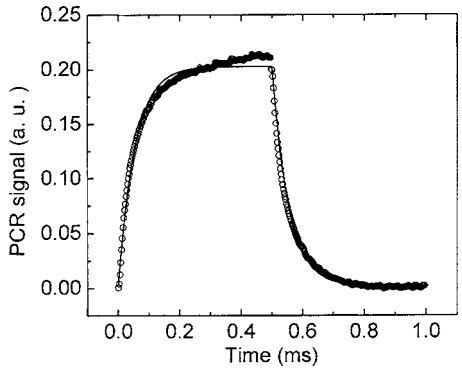

FIG. 4. Room-temperature experimental and best-fitted PCR transient results for *p*-Si sample using transient PCR theory with an infinite pulse train, Eq. (22). Wafer thickness $x_0=502$ μm, $\tau_p=0.5$ ms, and $T_0=1$ ms. Other constants are $\lambda=500$ nm (corresponding to $\alpha\approx 10^4$ cm^{-1}) and $R_1\sim R_2=0.5$. Standard deviations are on the order of the size of the symbols and are not shown. Solid line: theoretical fit; circles: experimental data.

of the generator was fixed for each experiment and the repetition period T_0 was scanned ("path I") such that $T_0 \geqslant \tau_\rho$. The reference signal waveform was at the instantaneous frequency $f=1/T_0$. The LIA was set to operate in the in-phase (IP) and quadrature (Q) modes. A Si photodiode was used to monitor a small fraction of the time-gated optical waveform past the AOM and its output was connected to a Voltcraft model 652 (50 MHz) oscilloscope, which was triggered by the electrical waveform generator via a connection to its "sync out" port, in order to provide a visual trace of the optical photoexcitation waveform incident on the sample. This trace was further used for making base line corrections to PCR waveforms. In this manner, use of the two oscilloscopes allowed viewing both excitation and response waveforms at all times.

III. EXPERIMENTAL RESULTS

To fully understand the physics of the PCR rate-window signal generation process, the time-domain photoexcitation and recombination process from a semiconductor must be modeled. Toward this purpose, data were obtained at two stages of photoexcitation of the semiconductor samples: PCR transients as a result of direct pulse-train excitation at 50%

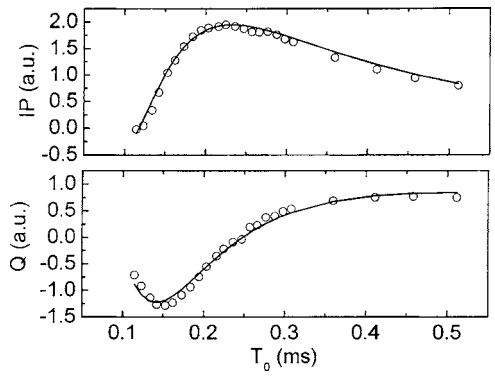

FIG. 5. Room-temperature experimental (circles) and best-fitted (lines) lock-in rate-window PCR results for *n*-Si sample using lock-in rate-window PCR theory with an infinite pulse train: $\tau_p=100$ μs, 100 μs$\leqslant T_0 \leqslant$500 μs, and $T=27$ °C. Standard deviations are on the order of the size of the symbols and are not shown.

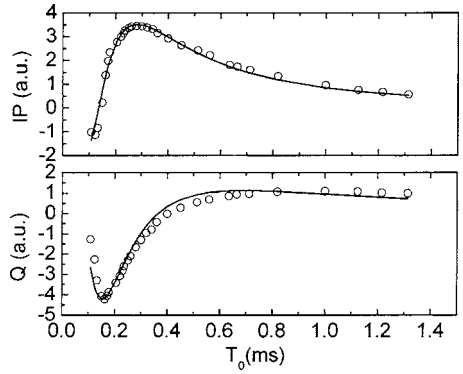

FIG. 6. Room-temperature experimental (circles) and best-fitted (lines) lock-in rate-window PCR results for *p*-Si sample using lock-in rate-window PCR theory with an infinite pulse train. $\tau_p=100$ μs, 100 $\mu s \leqslant T_0 \leqslant 1.4$ ms, and $T=27$ °C. Standard deviations are on the order of the size of the symbols and are not shown.

optical-pulse duty cycle, coadded over several hundreds of measurements, and IP- and *Q*-channel LIA rate-window scans of the repetition time T_0 with introduction of the PCR transients into the input of the lock-in amplifier. Figures 3 and 4 show the results of the PCR transients from the *n*-type and *p*-type Si wafers, respectively. It is noted that the PCR signals from the *n*-Si are of much lower quality (lower magnitude and compromised signal-to-noise ratio in both amplitude and phase channels) than those from the *p*-Si. The decay-time constant of the *n*-Si sample is also considerably shorter than that of the *p*-Si, as expected intuitively from an electronically poor material with a high defect/impurity density in which carriers deexcite mostly nonradiatively at the expense of radiative recombinations on which the PCR signal is based. These features are used as criteria for defining "electronically poor" or "electronically weak" semiconductors in the remainder of this work. These qualitative features are further borne out through quantitative fits to theoretical curves (Sec. IV) with results shown in Table I. Correspondingly, Figs. 5 and 6 show the LIA rate-window results, both IP and *Q* channels, as functions of the pulse repetition period T_0. Owing to the shorter characteristic decay-time constant of the *n*-Si sample, the time scale of the rate-window traces of this sample, Fig. 5, had to be shrunk to less than half of the time scale used for $T=78$-Si, Fig. 6. Additional rate-

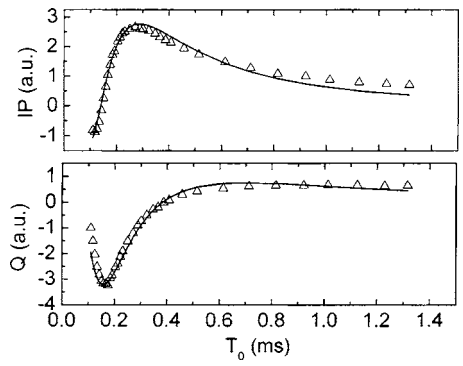

FIG. 7. $T=256$ C experimental and best-fitted lock-in rate-window PCR results for *p*-Si sample using lock-in rate-window PCR theory with an infinite pulse train. $\tau_p=100$ μs and 100 $\mu s \leqslant T_0 \leqslant 1.4$ ms. Solid line: theoretical fit; triangles: experimental data.

TABLE III. Fitted transport parameters of *n*-Si sample at various temperatures.

T (°C)	Front-surface recombination velocity (S_1)(cm/s)	Rear-surface recombination velocity (S_2)(cm/s)	Carrier-diffusion coefficient (D_p)(cm^2/s)	Carrier lifetime (τ)(μs)
23	264.2	2.7×10^4	25.9	12.4
78	243.7	3.1×10^4	22.9	16.6
176	224.6	2.8×10^4	19.5	20.3
256	212.3	2.9×10^4	14.4	25.6

window measurements were performed at elevated temperatures ($T=78$, 176, and 256 °C) on both Si samples. Figure 7 shows the results from the 256 °C run with the *p*-Si wafer. The experimental results were fitted to PCR rate-window theory (Sec. IV) and the resulting transport parameters are shown in Tables II and III. From comparisons between Figs. 3 and 5 and Figs. 4 and 6, it is clearly seen that rate-window detection of time-domain PCR signals through lock-in demodulation of the fundamental Fourier coefficient of the transient[21] can be far superior to directly coadded transients, especially when very low-level, noisy signals from electronically poor semiconductors are concerned, such as those in Fig. 3. In Table I literature values of the relevant diffusion coefficients and recombination lifetimes for *p*- and *n*-type Si have been given for comparison purposes with the present results. It should be remembered that the measured values are for ambipolar diffusivities which lie in between the pure D_p and D_n values reported in the literature.

IV. THEORY

A. Time-domain impulse-response excess free-carrier theory

Figure 8 shows a cross section of a one-dimensional PCR signal generation geometry, valid in the limit of large incident laser beams compared to the carrier-diffusion length[13] L_D and/or sample thickness x_0 (whichever is larger). This arrangement with the coordinate system centered in the middle of the semiconductor can be reduced to a fully symmetric geometry in the limits of equal surface reflectivities R_1 and R_2 and recombination velocities S_1 and S_2, and in that limit it may thus be directly compared to that case.[10] A radiation intensity I_0 (W m^{-2}) consisting of super-band-gap photons of energy $\hbar\omega$ is incident on the semiconductor surface at $x=-x_0/2$. The PCR time-domain problem can be ex-

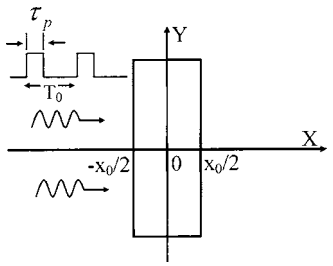

FIG. 8. Cross section of one-dimensional geometry for PCR signal generation in a semiconductor with thickness x_0 on which an incident laser-pulse wave train of duration τ_p and repetition period T_0 impinge.

pressed in terms of the simplest boundary- and initial-value problems for the excess minority-carrier density, e.g., excess holes in an n-type Si wafer, $\Delta p(x,t)$. This excess free photoexcited carrier density can be described as the response to an optical impulse $I(t)=I_0\delta(t)$:

$$D_p\frac{\partial^2\Delta p(x,t)}{\partial x^2}-\frac{\Delta p(x,t)}{\tau}=\frac{\partial\Delta p(x,t)}{\partial t}, \tag{1}$$

$$D_p\frac{\partial\Delta p(x,t)}{\partial x}\bigg|_{x=-1/2^{x_0}}=S_1\Delta p\left(-\frac{1}{2}x_0,t\right), \tag{2}$$

$$-D_p\frac{\partial\Delta p(x,t)}{\partial x}\bigg|_{x=1/2^{x_0}}=S_2\Delta p\left(\frac{1}{2}x_0,t\right), \tag{3}$$

$$\Delta p(x,0)=\frac{I_0\alpha(1-R_1)}{\hbar\omega}\left\{\frac{e^{-\alpha(x+1/2^{x_0})}+R_2e^{-\alpha[x_0-(x-1/2^{x_0})]}}{1-R_1R_2e^{-2\alpha x_0}}\right\}. \tag{4}$$

Physically, the incident radiation impulse at $t=0$ is absorbed by the sample with an absorption coefficient α at the excitation wavelength. It undergoes infinite inter-reflections across the two air-semiconductor interfaces and results in an initial free photocarrier distribution given by Eq. (4). Here D_p is the ambipolar carrier diffusivity and τ is the carrier recombination lifetime in the bulk of the semiconductor. The diffusion length is defined as[22] $L_D=(D_p\tau)^{1/2}$. Use of conventional separation of variables yields the general expression for the time-dependent excess hole density in the semiconductor

$$\Delta p(x,t)=e^{-t/\tau}\sum_{m=1}^{\infty}\{e^{-\lambda_m{}^2D_p t}[A_{1m}\cos(\lambda_m x)+A_{2m}\sin(\lambda_m x)] + e^{-\mu_m{}^2D_p t}[B_{1m}\cos(\mu_m x)+B_{2m}\sin(\mu_m x)]\}. \tag{5}$$

In view of Eq. (5), Eq. (4) may also be written as

$$\Delta p(x,0)=\sum_{m=1}^{\infty}[A_{1m}\cos(\lambda_m x)+A_{2m}\sin(\lambda_m x) + B_{1m}\cos(\mu_m x)+B_{2m}\sin(\mu_m x)]. \tag{6}$$

In Eq. (5) the expressions inside the two superposition brackets represent eigenfunctions of the boundary-value problem, Eqs. (1)–(3). λ_m and μ_m are the associated eigenvalues. The spatial eigenfunctions of the boundary-value problem are by definition orthogonal;[23] they must be normalized, and therefore are written as

$$\Psi_m(x)=C_{1m}(\lambda_m)[\cos(\lambda_m x)+(b_m/a_m)\sin(\lambda_m x)], \tag{7a}$$

$$\Phi_m(x)=C_{2m}(\mu_m)[(c_m/d_m)\cos(\mu_m/x)+\sin(\mu_m x)]. \tag{7b}$$

The boundary conditions, Eqs. (2) and (3), give the problem a degree of symmetry and yield the following expressions for the integration constants in Eqs. (7):

$$a_m(z_m)=c_m(z_m)=S_1\sin(z_m x_0/2)+D_p z_m\cos(z_m x_0/2), \tag{8a}$$

$$b_m(z_m)=d_m(z_m)=S_1\cos(z_m x_0/2)-D_p z_m\sin(z_m x_0/2). \tag{8b}$$

Here z_m stands for either eigenvalue λ_m or μ_m. The symmetric arrangement of the boundary-value problem with respect to the origin $x=0$ of the solid, Fig. 8, is such that the set of eigenfunctions $\{\Psi_m(x)\}$ represents symmetric (or even) solutions about the origin with corresponding eigenvalues $\{\lambda_m\}$, whereas the set $\{\Phi_m(x)\}$ represents antisymmetric (or odd) solutions with corresponding eigenvalues $\{\mu_m\}$. The requirement for simultaneous satisfaction of boundary conditions (2) and (3) under the general solution, Eq. (5), yields the following eigenvalue equation:

$$\sin\left(\frac{1}{2}\lambda x_0-\nu_1\right)\cos\left(\frac{1}{2}\lambda x_0-\nu_2\right) + \cos\left(\frac{1}{2}\lambda x_0-\nu_1\right)\sin\left(\frac{1}{2}\lambda x_0-\nu_2\right)=0, \tag{9a}$$

where λ is the eigenvalue and ν_1, ν_2 are defined as follows:

$$\cos\nu_j=\frac{D_p\lambda}{\sqrt{(D_p\lambda)^2+S_j^2}},\quad \sin\nu_j=\frac{S_j}{\sqrt{(D_p\lambda)^2+S_j^2}}, \tag{9b}$$

$$j=1,2.$$

The eigenvalue equation can be further decomposed into two linearly independent transcendental equations which together cover the full spectrum of eigenvalues in the form of two independent sets:

$$\cot\left(\frac{1}{2}\lambda_m x_0\right)=F\left(\frac{1}{2}\lambda_m x_0\right)+\sqrt{1+F^2\left(\frac{1}{2}\lambda_m x_0\right)}, \tag{10a}$$

$$m=1,2,3,\ldots,$$

and

$$\tan\left(\frac{1}{2}\mu_m x_0\right)=-F\left(\frac{1}{2}\mu_m x_0\right)-\sqrt{1+F^2\left(\frac{1}{2}\mu_m x_0\right)}, \tag{10b}$$

$$m=1,2,3,\ldots,$$

where

$$F(y) \equiv \frac{2D_p}{(S_1+S_2)x_0}\left[y - S_1S_2\left(\frac{x_0}{2D_p}\right)^2\frac{1}{y}\right]. \tag{10c}$$

Through some trigonometric manipulation, the second eigenvalue equation can be written in a form symmetric with respect to the first eigenvalue equation, Eq. (10a):

$$\cot\left(\frac{1}{2}\mu_m x_0\right) = F\left(\frac{1}{2}\mu_m x_0\right) - \sqrt{1+F^2\left(\frac{1}{2}\mu_m x_0\right)}, \tag{10d}$$

$$m = 1,2,3,\ldots.$$

In the limit of equal front- and back-surface recombination velocities, $S_1=S_2=S$, it can be shown that the symmetric eigenvalue equation (10a) reduces to the simple transcendental form

$$\cot\left(\frac{1}{2}\lambda_m x_0\right) = \frac{D_p\lambda_m}{S}. \tag{11a}$$

This equation has been derived by Luke and Cheng[10] in their treatment of the symmetric boundary-value problem of Eqs. (1)–(3) with equal surface recombination velocities. The result is the symmetric (even) solutions of Ref. 10, Appendix Eq. (A10). Similarly, Eq. (10b) reduces to

$$\tan\left(\frac{1}{2}\mu_m x_0\right) = -\frac{D_p\mu_n}{S}, \tag{11b}$$

which was also derived by Luke and Cheng[10] and leads to the antisymmetric (odd) solutions of Ref. 10, Appendix Eq. (A11).

Now, the normalization constants C_{1m} and C_{2m} of the eigenfunctions, Eqs. (7a) and (7b), can be determined from the initial condition (6) which is written with the use of Eqs. (8a) and (8b) as

$$\begin{aligned}\Delta p(x,0) = \sum_{m=1}^{\infty}\{&C_{1m}\{\cos(\lambda_m x) \\ &+ [b_m(\lambda_m)/a_m(\lambda_m)]\sin(\lambda_m x)\} \\ &+ C_{2m}\{[a_m(\mu_m)/b_m(\mu_m)]\cos(\mu_m x) \\ &+ \sin(\mu_m x)\}\}.\end{aligned} \tag{12}$$

Using the initial condition, Eq. (4), and the orthogonality property of the eigensets $\{\Psi_m(x)\}$ and $\{\Phi_m(x)\}$ (both intraset and interset orthogonalities), multiplying both sides in Eq. (12) by $\Psi_n(x)$ and integrating over the spatial domain of definition, one obtains

$$\begin{aligned}K\int_{-x_0/2}^{x_0/2}\{e^{-\alpha(x+x_0/2)} + R_2e^{-\alpha[(3x_0/2)-x]}\}&[a_n\cos(\lambda_n x) \\ + b_n\sin(\lambda_n x)]dx &= C_{1n}\int_{-x_0/2}^{x_0/2}[\cos(\lambda_n x) \\ + (b_n/a_n)\sin(\lambda_n x)]^2dx, \quad K &\equiv \frac{I_0\alpha(1-R_1)}{\hbar\omega(1-R_1R_2e^{-2\alpha x_0})}.\end{aligned} \tag{13}$$

Here, $a_n(\lambda_n)$ and $b_n(\lambda_n)$ are known coefficients given by Eqs. (8). Carrying out the integrations on both sides is straightforward, albeit tedious, and solving for C_{1n} gives

$$C_{1n}(\lambda_n) = \frac{4K\lambda_n a_n(a_nf_{1n} - b_nf_{2n})e^{-\alpha x_0/2}}{(\alpha^2+\lambda_n^2)\{a_n^2[\lambda_n x_0 + \sin(\lambda_n x_0)] + b_n^2[\lambda_n x_0 - \sin(\lambda_n x_0)]\}}, \tag{14a}$$

$$a_n = a_n(\lambda_n), \quad b_n = b_n(\lambda_n),$$

where the following function definitions were made:

$$f_{1n}(\lambda_n) \equiv (1+R_2e^{-\alpha x_0})\left[\alpha\sinh\left(\frac{1}{2}\alpha x_0\right)\cos\left(\frac{1}{2}\lambda_n x_0\right) + \lambda_n\cosh\left(\frac{1}{2}\alpha x_0\right)\sin\left(\frac{1}{2}\lambda_n x_0\right)\right], \tag{14b}$$

$$f_{2n}(\lambda_n) \equiv (1-R_2e^{-\alpha x_0})\left[\alpha\cosh\left(\frac{1}{2}\alpha x_0\right)\sin\left(\frac{1}{2}\lambda_n x_0\right) - \lambda_n\sinh\left(\frac{1}{2}\alpha x_0\right)\cos\left(\frac{1}{2}\lambda_n x_0\right)\right]. \tag{14c}$$

It is worth noting that if $S_1=S_2=S$, then $b_n(\lambda_n)=0$ in Eqs. (8); this reduces C_{1n} to the coefficient A_n, Eq. (1d), Ref. 10, as expected in the fully symmetric case.

Repeating the foregoing procedure, multiplying both sides of Eq. (12) by a member of the odd eigenset, $\Phi_n(x)$, and integrating over the spatial domain of definition, one obtains

$$C_{2n}(\mu_n) = \frac{4K\mu_n b_n(a_nf_{1n} - b_nf_{2n})e^{-\alpha x_0/2}}{(\alpha^2+\mu_n^2)\{a_n^2[\mu_n x_0 + \sin(\mu_n x_0)] + b_n^2[\mu_n x_0 - \sin(\mu_n x_0)]\}}, \tag{15a}$$

$$f_{1n} = f_{1n}(\mu_n), \quad f_{2n} = f_{2n}(\mu_n), \quad a_n = a_n(\mu_n), \quad b_n = b_n(\mu_n). \tag{15b}$$

In this case, if $S_1=S_2=S$, then $a_n(\mu_n)=0$ in Eqs. (8); Eq. (15) immediately reduces to the coefficient B_n, Eq. (1e), Ref. 10, as expected. Finally, collecting all terms, Eq. (5) can be solved in terms of the parameters derived from the eigenvalue equations (10a)–(10d) and also defined in Eqs. (8), (14), and (15):

$$\Delta p(x,t) = e^{-t/\tau}\sum_{n=1}^{\infty}\left\{C_{1n}(\lambda_n)\left[\cos(\lambda_n x) + \frac{b_n(\lambda_n)}{a_n(\lambda_n)}\sin(\lambda_n x)\right]e^{-\lambda_m{}^2 D_{p'}t} + C_{2n}(\mu_n) \times\left[\frac{a_n(\mu_n)}{b_n(\mu_n)}\cos(\mu_n x) + \sin(\mu_n x)\right]e^{-\mu_m{}^2 D_{p'}t}\right\}. \quad (16)$$

An important special case is that of an optically opaque semiconductor at the excitation wavelength, i.e., when $\alpha x_0 \gg 1$, i.e., $\exp(-\alpha x_0)\sim 0$. In this limit which represents realistic conditions for visible-light excitation of commercial Si wafers, the coefficients C_{1n} and C_{2n} in Eqs. (14) and (15) become independent of the optical-absorption coefficient α (photocarrier radiometry optical saturation regime):

$$C_{1n}(\lambda_n) = \frac{2I_0(1-R_1)a_n[a_n\cos(\lambda_n x_0/2) - b_n\sin(\lambda_n x_0/2)]}{\hbar\omega\{a_n{}^2[\lambda_n x_0 + \sin(\lambda_n x_0)] + b_n{}^2[\lambda_n x_0 - \sin(\lambda_n x_0)]\}}, \quad (16a)$$

$$C_{2n}(\mu_n) = \frac{2I_0(1-R_1)b_n[a_n\cos(\mu_n x_0/2) - b_n\sin(\mu_n x_0/2)]}{\hbar\omega\{a_n{}^2[\mu_n x_0 + \sin(\mu_n x_0)] + b_n{}^2[\mu_n x_0 - \sin(\mu_n x_0)]\}}. \quad (16b)$$

B. Time-domain excess free-carrier theory: Optical square pulse-train excitation

The carrier-density impulse-response $\Delta p(x,t)$, Eq. (5), can be transformed to account for a square-wave excitation pulse of duration τ_p. If, instead of the optical impulse $I(t) = I_0\delta(t)$, the finite square pulse

$$I(t) = I_0\begin{cases}1; 0 \leqslant t < \tau_p\\ 0; t > \tau_p\end{cases} \quad (17)$$

is incident on the surface of a semiconductor, the convolution theorem can be used to obtain the transient response from the impulse response, Eq. (16):

$$\Delta p_1(x,t) = \int_0^t I(\tau)\Delta p(x,t-\tau)d\tau = \int_0^t \Delta p(x,t-\tau)d\tau, \quad 0 \leqslant t \leqslant \tau_p, \quad (18a)$$

$$\Delta p_1(x,t) = \int_0^{\tau_p} I(\tau)\Delta p(x,t-\tau)d\tau = \int_0^{\tau_p} \Delta p(x,t-\tau)d\tau, \quad t \geqslant \tau_p. \quad (18b)$$

The resulting expressions are

$$\Delta p_1(x,t) = \sum_{n=1}^{\infty}\left\{C_{1n}(\lambda_n)\tau_{1n}\left[\cos(\lambda_n x) + \frac{b_n(\lambda_n)}{a_n(\lambda_n)}\sin(\lambda_n x)\right] \times(1 - e^{-t/\tau_{1n}}) + C_{2n}(\mu_n)\tau_{2n}\left[\frac{a_n(\mu_n)}{b_n(\mu_n)}\cos(\mu_n x) + \sin(\mu_n x)\right](1 - e^{-t/\tau_{2n}})\right\}, \quad 0 \leqslant t \leqslant \tau_p \quad (19a)$$

and

$$\Delta p_1(x,t) = \sum_{n=1}^{\infty}\left\{C_{1n}(\lambda_n)\tau_{1n}\left[\cos(\lambda_n x) + \frac{b_n(\lambda_n)}{a_n(\lambda_n)}\sin(\lambda_n x)\right] \times(e^{\tau_p/\tau_{1n}} - 1)e^{-t/\tau_{1n}} + C_{2n}(\mu_n)\tau_{2n}\left[\frac{a_n(\mu_n)}{b_n(\mu_n)}\cos(\mu_n x) + \sin(\mu_n x)\right] \times(e^{\tau_p/\tau_{2n}} - 1)e^{-t/\tau_{2n}}\right\}, \quad t \geqslant \tau_p. \quad (19b)$$

The foregoing expressions are indicative of linear superpositions of rise- or decay-time modes with characteristic time constants equal to

$$\tau_{1n}^{-1} \equiv \tau^{-1} + \lambda_n{}^2 D_p, \quad \tau_{2n}^{-1} \equiv \tau^{-1} + \mu_n{}^2 D_p. \quad (20)$$

It is seen that each mode rises or decays with a composite time constant comprising both bulk recombination lifetime and surface recombination lifetime which depends on the eigenvalues λ_n and μ_n. The latter are functions of the surface recombination velocities through the eigenvalue equations (10a) and (10d) and their dependence on function F, Eq. (10c).

The free-carrier-density transient due to a single square-wave pulse can be generalized to include the effects of an infinite train of prior pulses before the onset of the current transient. Upon summing up the effects of all prior pulses, Eqs. (19a) and (19b) will be modified as follows:

$$\Delta p_\infty(x,t)\big|_{t=(m-1)T_0\to\infty} = \sum_{n=1}^{\infty}\left[g_{1n}(x;\lambda_n)\tau_{1n}\left(\frac{e^{\tau_p/\tau_{1n}} - 1}{1 - e^{-T_0/\tau_{1n}}}\right)e^{-T_0/\tau_{1n}} + g_{2n}(x;\mu_n)\tau_{2n}\left(\frac{e^{\tau_p/\tau_{2n}} - 1}{1 - e^{-T_0/\tau_{2n}}}\right)e^{-T_0/\tau_{2n}}\right], \quad (21a)$$

where the following definitions were made:

$$g_{1n}(x;\lambda_n) \equiv C_{1n}(\lambda_n)\left[\cos(\lambda_n x) + \frac{b_n(\lambda_n)}{a_n(\lambda_n)}\sin(\lambda_n x)\right] \quad (21b)$$

and

$$g_{2n}(x;\mu_n) \equiv C_{2n}(\mu_n)\left[\frac{a_n(\mu_n)}{b_n(\mu_n)}\cos(\mu_n x) + \sin(\mu_n x)\right]. \quad (21c)$$

Finally, at time Δt after the end of an infinite pulse train, $t = (m-1)T_0 \to \infty$, such that during the current mth pulse, $0 \leqslant \Delta t \leqslant T_0$, we may superpose all the contributions due to the prior pulse train and the effects of the current pulse:

$$p(x,\Delta t)=\Delta p_\infty(x,\infty;\Delta t)+\Delta p_1(x,\Delta t)=\sum_{n=1}^{\infty}\sum_{j=1}^{2} g_{jn}(x)\tau_{jn}\begin{cases}1-\left(\frac{e^{T_0/\tau_{jn}}-e^{\tau_p/\tau_{jn}}}{e^{T_0/\tau_{jn}}-1}\right)e^{-\Delta t/\tau_{jn}}, & 0\leqslant\Delta t\leqslant\tau_p\\ \left(\frac{e^{\tau_p/\tau_{jn}}-1}{e^{T_0/\tau_{jn}}-1}\right)e^{T_0/\tau_{jn}}e^{-\Delta t/\tau_{jn}}, & \tau_p\leqslant\Delta t\leqslant T_0.\end{cases} \tag{22}$$

C. Time-domain and lock-in rate-window PCR signals

The PCR signal in the usual case of relatively low infrared optical-absorption coefficient distribution within the spectral range of the InGaAs (or any other near-IR) detector is given by the spatial depth integral of the photoexcited excess carrier density recombining radiatively in impurity or defect states in the band gap of the semiconductor.[16] For an infinite pulse train generating the excess carrier density $p(x,\Delta t)$ of Eq. (22), we obtain

$$S_\infty(\Delta t)=\text{const}\times\int_{-x_0/2}^{x_0/2}p(x,\Delta t)dx. \tag{23}$$

Here, the constant is a function of the reflection coefficients at the sample interfaces, the carrier capture cross sections, the probability for radiative emission following a recombination event, the spectral bandwidth of the IR detector, and various instrumental factors. Owing to spatial averaging the antisymmetric modes vanish, as $\int_{-x_0/2}^{x_0/2}\sin(\lambda_n x)dx=0$. Therefore, only the symmetric modes contribute, giving a PCR signal which can be written as

$$S_\infty(t)=\text{const}\times\sum_{n=1}^{\infty}\sum_{j=1}^{2}H_{jn}(\lambda_n{}^j)\tau_{jn}\begin{cases}1-\left(\frac{e^{T_0/\tau_{jn}}-e^{\tau_p/\tau_{jn}}}{e^{T_0/\tau_{jn}}-1}\right)e^{-t/\tau_{jn}}, & 0\leqslant t\leqslant\tau_p\\ \left(\frac{e^{\tau_p/\tau_{jn}}-1}{e^{T_0/\tau_{jn}}-1}\right)e^{T_0/\tau_{jn}}e^{-t/\tau_{jn}}, & \tau_p\leqslant t\leqslant T_0,\end{cases} \tag{24}$$

where, compactly, $\lambda_n{}^1=\lambda_n$ and $\lambda_n{}^2=\mu_n$; also, from Eqs. (16):

$$H_{1n}(\lambda_n)\equiv\frac{1}{\lambda_n}C_{1n}(\lambda_n)\sin\left(\frac{1}{2}\lambda_n x_0\right), \tag{24a}$$

$$H_{2n}(\mu_n)\equiv\frac{1}{\mu_n}\left[\frac{a_n(\mu_n)}{b_n(\mu_n)}\right]C_{2n}(\mu_n)\sin\left(\frac{1}{2}\mu_n x_0\right). \tag{24b}$$

These expressions represent the PCR emissions at any instant, t, during a given period T_0, to which all prior pulses are contributing, especially in cases of long lifetimes where there is going to be inevitable overlap of signals from one period to the next, or across several periods. Now, the rate-window signal in the lock-in amplifier IP channel can be written as[14,21]

$$S_{\text{PCR}}^{(\text{IP})}(T_0)=\frac{2\omega_0}{\pi^2}\int_0^{T_0}S_\infty(t)\sin(\omega_0 t)dt=\text{const}\times\sum_{n=1}^{\infty}\sum_{j=1}^{2}H_{jn}(\lambda_n{}^j)J_{jn}^{(\text{IP})}(\tau_{jn};\tau_p,T_0), \tag{25}$$

where $\omega_0=2\pi/T_0$ and

$$J_{jn}^{(\text{IP})}(\tau_{jn};\tau_p,T_0)\equiv\tau_{jn}[1-\cos(\omega_0\tau_p)+\{[G_1(\tau_{jn})e^{-\tau_p/\tau_{jn}}+G_2(\tau_{jn})e^{(T_0-\tau_p)/\tau_{jn}}]\sin(\omega_0\tau_p+\theta_{jn})-[G_1(\tau_{jn})+G_2(\tau_{jn})]\sin\theta_{jn}\}\sin\theta_{jn}],\quad j=1,2. \tag{26}$$

Here, the following definitions were made:

$$G_1(\tau_{jn})\equiv\frac{e^{T_0/\tau_{jn}}-e^{\tau_p/\tau_{jn}}}{e^{T_0/\tau_{jn}}-1},\quad G_2(\tau_{jn})\equiv\frac{e^{\tau_p/\tau_{jn}}-1}{e^{T_0/\tau_{jn}}-1}, \tag{26a}$$

$$\sin\theta_{jn}=\frac{\omega_0}{\sqrt{\tau_{jn}^{-2}+\omega_0{}^2}},\quad\cos\theta_{jn}=\frac{\tau_{jn}^{-1}}{\sqrt{\tau_{jn}^{-2}+\omega_0{}^2}}. \tag{26b}$$

In the limit of $\tau_{jn}\ll(T_0,\tau_p)$, there should be negligible overlap between successive PCR transient wave forms. In that case, $G_1(\tau_{jn})+G_2(\tau_{jn})\cong 1-\exp(-T_0/\tau_{jn})\cong 1$. Inserting this value in Eqs. (26) we see that only the term $n=1$ survives with $\exp(-T_0/\tau_{jn})\approx 0$ and the equation reduces to the single-pulse result reported by Chen *et al.*[15]

Finally, the rate-window signal in the lock-in amplifier Q channel can be written as[14,21]

$$S_{\text{PCR}}^{(Q)}(T_0)=\frac{2\omega_0}{\pi^2}\int_0^{T_0}S_\infty(t)\cos(\omega_0 t)dt=\text{const}\times\sum_{n=1}^{\infty}\sum_{j=1}^{2}H_{jn}(\lambda_n{}^j)J_{jn}^{(Q)}(\tau_{jn};\tau_p,T_0), \tag{27}$$

where

$$J_{jn}^{(Q)}(\tau_{jn};\tau_p,T_0)\equiv\tau_{jn}[\sin(\omega_0\tau_p)+\{[G_1(\tau_{jn})e^{-\tau_p/\tau_{jn}}+G_2(\tau_{jn})e^{(T_0-\tau_p)/\tau_{jn}}]\cos(\omega_0\tau_p+\theta_{jn})-[G_1(\tau_{jn})+G_2(\tau_{jn})]\cos\theta_{jn}\}\sin\theta_{jn}],\quad j=1,2. \tag{27a}$$

V. SELECTED SIMULATIONS OF PCR TRANSIENT AND RATE-WINDOW WAVE FORMS

Theoretical PCR transient wave forms obtained from Eqs. (24) using the eigenvalue equations (10a) and (10d), coefficients (a_n,b_n) from Eqs. (8), and coefficients C_{1n} and C_{2n} from Eqs. (16a) and (16b) were calculated for typical p-Si electronic transport parameters. The numerical simula-

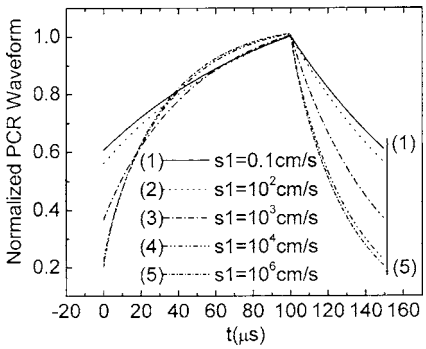

FIG. 9. Time-domain infinite-pulse-train PCR transients normalized to the maximum value with front-surface recombination velocity, S_1, as a parameter. S_2=0.1 cm/s, τ=100 μs, D_p=30 cm^2/s, τ_p=100 μs, and x_0=600 μm. Other constants are λ=500 nm (corresponding to $\alpha \approx 10^4$ cm^{-1}) and $R_1 \sim R_2$=0.5.

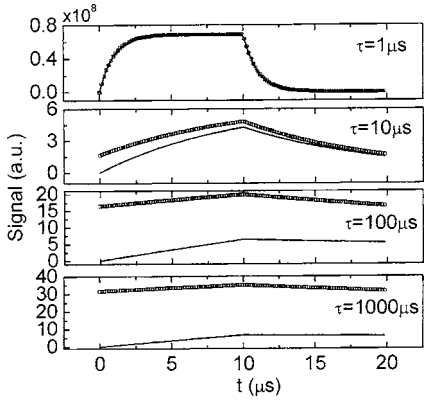

FIG. 10. Comparison between single-pulse and infinite-pulse responses with various bulk lifetime τ values as a parameter. Solid line: single-shot transient; hollow squares: transient following an infinite prior pulse train. S_1 =10 cm/s, S_2=1000 cm/s, τ_p=10 μs, D_p=30 cm^2/s, and x_0=600 μm.

tions were performed using MATLAB. The eigenvalue equations for λ_m, Eq. (10a), and for μ_m, Eq. (10d), were numerically solved by finding the zeros of the function which is equal to the difference between the left-hand side and the right-hand side of Eqs. (10a) and (10d), respectively. Figure 9 shows the results of the time-domain waveform dependence on the front-surface recombination velocity, S_1. From these and other simulations involving a single PCR pulse, it can be concluded that increasing S_1 has the effect of steepening both excess carrier generation (rise-time) and recombination (decay-time) profiles. Comparison with single-pulse responses shows that the incidence/superposition of prior pulses affects the current wave form, $0 \leqslant t \leqslant T_0$, for $S_1 \leqslant 1000$ cm/s. In this case, the onset of each new pulse occurs at values above the base line (zero) as earlier pulses are still decaying within the current pulse time interval. In the simulation of Fig. 9 this happens at times shorter than the cutoff τ_p of the optical pulse: all single-pulse decays essentially coincide with the full pulse-train decay profile, as the effect of all prior pulses becomes negligible. It is noted that these differences essentially disappear when $t \gg \max(\tau_{j1}, \tau)$ (the eigenvalue equations always yield $\tau > \tau_{j1} > \tau_{j2} > \cdots > \tau_{jn}$). In this context, τ_{jn} plays the role of the effective (i.e., measurable) recombination lifetime of the nth decay mode, a combination of a symmetric and antisymmetric superposition of spatial modes. The effective lifetime controls the PCR pulse profile regardless of the duration and shape of the excitation laser pulse, as seen by the convolution equations (18). Effective lifetimes consist of the bulk lifetime and an effective surface recombination lifetime which, through the eigenvalue equations, involves the two surface recombination velocities and the ambipolar carrier diffusivity.

Similar trends to those shown in Fig. 9 are observed in simulations where the back-surface recombination velocity, S_2, is a variable parameter. The results are not reported here. Simulations with the bulk lifetime τ as a parameter are shown in Fig. 10. In this figure actual simulations of both single-pulse and infinite-pulse-train transients are shown. Comparison with the respective single-pulse transients reveals that the effects of increasing bulk lifetime are readily measurable for values of $\tau \geqslant T_0$, or, equivalently, for $\omega_0 \tau \geqslant 2\pi$. This is an important conclusion, in view of the fact that using harmonic PCR measurements,[16] the effects of bulk lifetime diminish and tend to saturate out as $\omega_0 \tau \gg 1$ by virtue of the $\omega_0 \tau$ dependence of the carrier wave number. Therefore, it is clear that the Fourier decomposition of the infinite-pulse-train time-domain PCR signal can be used as complementary to harmonic excitation to yield lifetime values which otherwise would be saturated out in the frequency domain. Figure 10 further shows that the prior pulse-train contributions to the current PCR response become increasingly more important for bulk recombination lifetime values such that $\tau > \tau_p$. Unless taken into account, prior pulse-train contributions could result in inaccurate measurements of τ, as shown in the cases τ=10, 100, and 1000 μs in that figure.

Figure 11 shows simulations of the effects of sample thickness on the infinite-pulse PCR transient. As thickness increases so does the intensity of the PCR pulse. Significantly, the effective decay lifetime increases as expected physically from the fact that in thicker samples the effects of back surface as a locus of recombination become less significant over one repetition period, thus increasing the density of free photoexcited carriers and delaying the overall recombination process as represented by the longest effective lifetime τ_{j1}, Eq. (20). It is well known[10] that at late times of the carrier-density decay profile, the decay mode with the longest effective lifetime, τ_{j1}, n=1, prevails over all higher

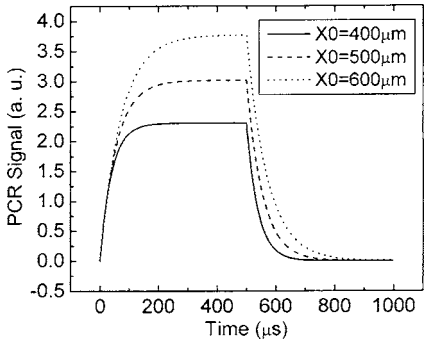

FIG. 11. Infinite-pulse-train time-domain-simulated PCR signals with thickness x_0 as a parameter. S_1=150 cm/s, S_2=8000 cm/s, τ=450 μs, D_p =12 cm^2/s, and τ_p=0.5 ms. Other constants are λ=500 nm (corresponding to $\alpha \approx 10^4$ cm^{-1}) and $R_1 \sim R_2$=0.5.

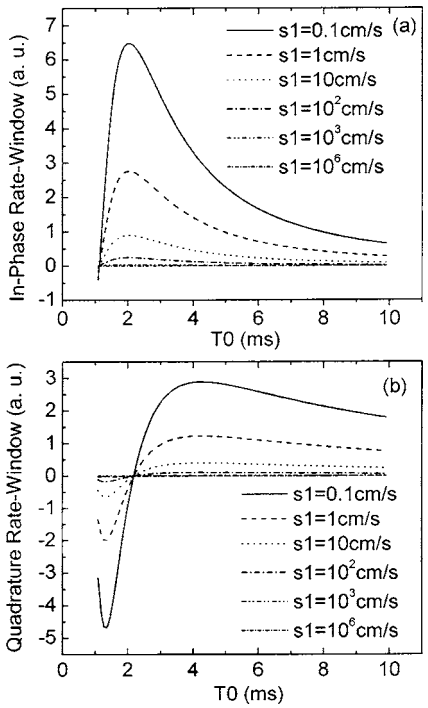

FIG. 12. Simulated in-phase (a) and quadrature (b) rate-window PCR signals with S_1 as a parameter. S_2=0.1 cm/s, τ=100 μs, D_p=30 cm^2/s, τ_p=1 ms, and x_0=600 μm. Other constants are λ=500 nm (corresponding to $\alpha \approx 10^4$ cm^{-1}) and $R_1 \sim R_2$=0.5.

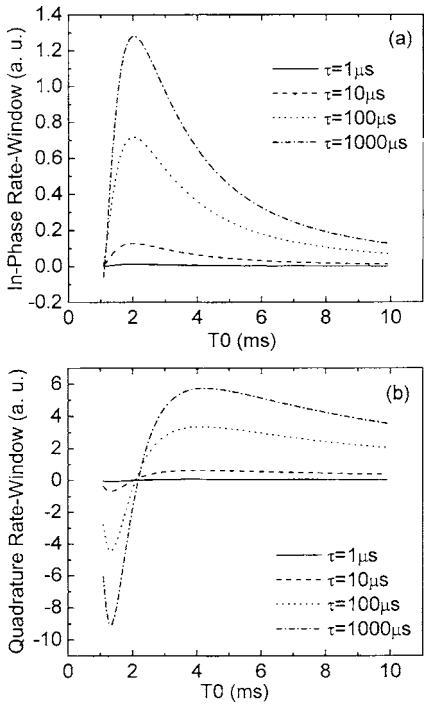

FIG. 13. Simulated in-phase (a) and quadrature (b) rate-window PCR signals with τ as a parameter. S_1=10 cm/s, S_2=1000 cm/s, D_p=30 cm^2/s, τ_p=1 ms, and x_0=600 μm. Other constants are λ=500 nm (corresponding to $\alpha \approx 10^4$cm^{-1}) and $R_1 \sim R_2$=0.5.

modes and a semilog plot of the transient produces a linear decay slope which depends on the thickness of the material. This characteristic behavior has led to several analytical techniques for bulk lifetime and surface recombination velocity extraction from the linear portions of data curves in photoluminescence[4,10,24] and cathodoluminescence[25] experiments. For the asymmetric boundary conditions of Eqs. (2) and (3) it is seen from the transient waveform of Eqs. (19a) and (19b) that the absolute magnitude of the nth mode decreases through the coefficients $C_{1n}(\lambda_n) \sim \lambda_n/(\alpha^2+\lambda_n^2)$ and $C_{2n}(\mu_n) \sim \mu_n/(\alpha^2+\mu_n^2)$ as the eigenvalues increase. At the same time, the time constant of the decay of each mode, $\exp(-t/\tau_{1n})$ and $\exp(-t/\tau_{2n})$, decreases leading to the acceleration of the decay (damping) of higher modes. In this respect, the frequency-domain approach[16] is simpler as it avoids involving the entire eigenvalue spectrum of the boundary-value problem in the measurement of transport properties, through externally driven single-mode excitation. That level of simplicity is achieved, however, at the expense of the uniqueness and sensitivity of the solution to the transport properties of the semiconductor.[26]

The reshaping of repetitive transient waveforms by the period-scanned lock-in amplifier rate-window process as experimentally implemented with the setup of Fig. 1 is shown in Fig. 12 as a function of T_0 with S_1 as a parameter. Similar effects are observed when the back-surface recombination velocity is varied. *Increasing* S_1 has effects on the shape of the rate-window PCR curve, Fig. 12, similar to those of *decreasing* bulk lifetime, Fig. 13. Figure 14 shows both single-pulse and infinite-pulse-train rate-window T_0 scans for various pulse durations. It is instructive to notice the strong effect of the pulse duration on the position of the peak in both IP and Q channels, as well as the significant waveform and peak shifts incurred when the infinite pulse train is unaccounted for, even for very short bulk lifetime (τ=10 μs). From these simulations it is clear that, if the effect of the infinite pulse train is not taken into account, false measurements of transport properties of the semiconductor will be made using the rate-window technique. This was also seen to be the case with time-domain transients, Figs. 9 and 10.

VI. TRANSIENT AND RATE-WINDOW PCR MEASUREMENTS OF SILICON TRANSPORT PROPERTIES

The solid line in Fig. 3 represents the theoretical fit of Eq. (22) to the PCR transient data from the *n*-type Si wafer. The data are of poor quality and quite noisy. The theoretical fit was done using MATLAB based on a least-squares method. The fitting process was performed automatically so that either a preset tolerance level was satisfied or a maximum number of iterations were reached. The experimental data were normalized by the optical waveform which was not exactly a square wave, as registered in the Voltcraft oscilloscope, Fig. 1. Transient-shape normalization was done through simple ratioing of the PCR output wave form by the line shape of the nearly square optical input waveform (not shown in Figs. 2 and 3). A mathematically more involved approach of the slightly skewed $I(t)$ optical waveform instead of the perfectly square-wave Eq. (17) could have been used in the convolution integrals of Eqs. (18a) and (18b), at considerable additional complexity without marked improvement in the calculations leading to the values shown in Tables I–III. Several hundreds of coadded PCR transients

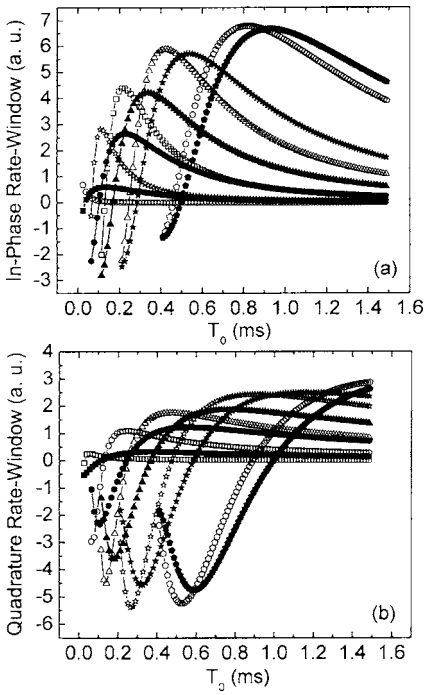

FIG. 14. Simulated in-phase (a) and quadrature (b) rate-window PCR signals with τ_p as a parameter. $S_1=10$ cm/s, $S_2=1000$ cm/s, $D_p=30$ cm^2/s, $x_0=600$ μm, $\tau=10$ μs: $\tau_p=10$ μs (squares), $\tau_p=50$ μs (circles), $\tau_p=100$ μs (triangles), $\tau_p=200$ μs (stars), and $\tau_p=400$ μs (pentagons). Full symbols: single-pulse PCR response, Eqs. (19a) and (19b); hollow symbols: infinite-pulse-train PCR response, Eq. (22). Other constants are $\lambda=500$ nm (corresponding to $\alpha\approx 10^4$ cm^{-1}) and $R_1\sim R_2=0.5$.

were averaged to produce the best possible signal-to-noise ratio. Figure 4 shows the equivalent results from the *p*-type Si wafer. For this sample the signal quality was much higher, resulting in a much better theoretical fit. However, the normalization correction to the optical waveform base line was not perfect, resulting in a degree of discrepancy between experimental and theoretical fits especially in the near-flat section of the transient: it was in the "pulse-on" time window that the optical waveform exhibited a slight positive slope which was not completely compensated with the simple ratio normalization. Using the infinite-pulse-train waveforms of Eqs. (25) and (27), the best-fit measurement results are shown in Table I. In the multiparameter fitting procedure, a mean-square variance defined as

$$V=\sum_P \left\{ \frac{\Sigma_{i=1}^N [A_T(t)-A_E(t)]^2}{\Sigma_{i=1}^N [A_E(t)]^2} \right\} \tag{28}$$

was minimized via least-squares procedure provided by MATLAB. Here $A_T(t)$ and $A_E(t)$ are the theoretical and the experimental PCR signals, respectively. P is the number of signal channels used in the fitting process. In the infinite-pulse transient operating mode, only one channel signal was obtained and used in the fitting, $P=1$. In the rate-window operating mode, both quadrature and in-phase signals were used in the fitting, $P=2$. N is the total number of data points in each channel. During the fitting process, the carrier lifetime, the carrier-diffusion coefficient, and the front- and rear-surface recombination velocities were set as free parameters to minimize the square variance V. Both time-domain transient and rate-window-derived parameters, Figs. 5 and 6, are very close to each other, with the advantage of significant improvements in signal-to-noise ratio of the latter.[21] The variance V of the transient signal for the *n*-type wafer was 1.5×10^{-2}. The variance V of the transient signal for the *p*-type wafer was 9.3×10^{-3}, as expected from the higher signal amplitude obtained from this wafer. Finally, the typical variance V of the lock-in rate-window signal was 2.1×10^{-3}, which justifies the superior performance of this signal generation technique. The rate-window high-temperature scans, typically represented by the best fits of Eqs. (25) and (27) to the data in Fig. 7, produced the measurements shown in Tables II and III for the *p*-type and *n*-type Si wafers, respectively. The major trends are the bulk lifetime increase and carrier ambipolar diffusivity decrease with increasing temperature. The trend in lifetime increase follows the Shockley-Read theory[27] which assumes that the thermally generated carrier density partially neutralizes existing trapping centers by increasing the occupation of empty defect and/or impurity energy states in the band gap. The trend in diffusivity decrease is consistent with the increase in scattering probabilities of free photoexcited carriers with increasing temperature affecting the diffusive recombination mean free path. These conclusions are also consistent with earlier frequency-domain PCR measurements of Si wafers.[28] On a semilogarithmic plot the onset of the purely linear portion of the decay curve in Fig. 3 commences at ca. 0.7 ms after the onset of the laser pulse, with the decay slope being steeper at earlier times following the end of the optical pulse. This behavior is borne out by the present time-domain PCR theory and has also been predicted by the Luke and Cheng model[10] for completely symmetric recombination conditions on both surfaces of a semiconductor. It is due to the contributions of the higher eigenmodes to the temporal profile which must be taken fully into account if accurate measurements of the bulk lifetime are desired. The rate-window methodology does that automatically with a superior SNR compared to time-domain PCR responses and appears to be preferable for these types of measurements, especially from weakly electronically active semiconductors. The complexities of the dual-slope method[10] can thus be totally avoided, especially in the more general and widely typical case where $S_1\neq S_2$ where that method may be inapplicable. The double-exponential curve fit of the radiative decay process of photocarriers used by Guidotti *et al.*,[19] who found two distinct and widely different PL decay times in Si subjected to a square-wave laser pulse, is another example of the need for adequate and careful theoretical modeling of these time-domain processes using the full eigenmode spectrum of the radiative recombination dynamics.

VII. CONCLUSIONS

Time-domain and lock-in rate-window photocarrier radiometry configurations were introduced both experimentally and theoretically to investigate the responses of *p*- and *n*-type Si wafers photoexcited by a square-wave-modulated super-band-gap laser beam. The solution to the complete asymmetric boundary-value problem with different recombi-

nation velocities at the two surfaces was developed and used to fit the time-domain data. The effects of the infinite prior pulse train to the current PCR waveform were quantified and were found to be very important for certain ranges of transport parameters, pulse durations, and repetition periods. Lock-in rate-window results retain the time-domain character of the photocarrier generation and recombination processes while being superior to coadded PCR transients especially in the case of an *n*-type Si sample with poor electronic carrier recombination characteristics. It is concluded that time-domain PCR detection at room temperature and above is sensitive to band-to-defect or band-to-impurity recombinations in Si, which are intrinsically long decay-time processes ($\geqslant 10\ \mu s$), as opposed to fast band-to-band recombination processes
($\sim 2.9\ \mu s$) which have been reported to date[11,17,19] under the generic label of room-temperature photoluminescence.

ACKNOWLEDGMENTS

One of the authors (A.M.) is grateful to the Alexander von Humboldt Foundation for a Research Award that made this work possible at Ruhr Universität Bochum. The authors wish to express their gratitude to Dietmar Krüger with heater design.

[1] J. A. Mroczkowski, J. F. Shanley, M. B. Reine, P. LoVecchio, and D. L. Polla, Appl. Phys. Lett. **38**, 261 (1981).
[2] S. M. Johnson and L. G. Johnson, J. Appl. Phys. **60**, 2008 (1986).
[3] Z. G. Ling and P. K. Ajmera, J. Appl. Phys. **69**, 519 (1991).
[4] G. S. Kousik, Z. G. Ling, and P. K. Ajmera, J. Appl. Phys. **72**, 141 (1992).
[5] R. Bernini, A. Cutolo, A. Irace, P. Spirito, and L. Zeni, Solid-State Electron. **39**, 1165 (1996).
[6] J. Waldmeyer, J. Appl. Phys. **63**, 1977 (1988).
[7] W. M. Bullis and H. R. Huff, J. Electrochem. Soc. **143**, 1399 (1996).
[8] W. van Roosbroeck, Phys. Rev. **91**, 282 (1953).
[9] A. Skumanich, D. Fournier, A. C. Boccara, and N. M. Amer, Appl. Phys. Lett. **47**, 402 (1985).
[10] K. L. Luke and L.-J. Cheng, J. Appl. Phys. **61**, 2282 (1987).
[11] D. Guidotti, J. S. Batchelder, A. Finkel, P. D. Gerber, and J. A. Van Vechten, J. Appl. Phys. **66**, 2542 (1989).
[12] B. Li, D. Shaughnessy, and A. Mandelis, J. Appl. Phys. **97**, 023701 (2005).
[13] A. Mandelis, *Diffusion-Wave Fields: Mathematical Methods and Green Functions* (Springer, New York, 2001), Chap. 9.
[14] A. Mandelis, R. Bleiss, and F. Shimura, J. Appl. Phys. **74**, 3431 (1993).
[15] Z. H. Chen, R. Bleiss, A. Mandelis, A. Buczkowski, and F. Shimura, J. Appl. Phys. **73**, 5043 (1993).
[16] A. Mandelis, J. Batista, and D. Shaughnessy, Phys. Rev. B **67**, 205208 (2003).
[17] O. King and D. G. Hall, Phys. Rev. B **50**, 10661 (1994).
[18] G. Kirchhoff, *Abhandlungen über Emission und Absorption*, edited by M. Planck (Engleman, Leipzig, 1898), pp. 11–36.
[19] D. Guidotti, J. S. Batchelder, J. A. Van Vechten, and A. Finkel, Appl. Phys. Lett. **48**, 68 (1986).
[20] W. Kurner, R. Sauer, A. Dornen, and K. Thonke, Phys. Rev. B **39**, 13327 (1989).
[21] A. Mandelis, Rev. Sci. Instrum. **65**, 3309 (1994).
[22] P. McKelvey, *Solid State and Semiconductor Physics* (Harper & Row, New York, 1969), Chap. 10.2.
[23] See, for example, V. S. Arpaci, *Conduction Heat Transfer* (Addison-Wesley, Reading, MA, 1966), Chap. 4.
[24] R. Bernini, A. Cutolo, A. Irace, P. Spirito, and I. Zeni, Solid-State Electron. **39**, 1165 (1996).
[25] M. Boulou and D. Bois, J. Appl. Phys. **48**, 4713 (1977).
[26] B. Li, D. Shaughnessy, and A. Mandelis, J. Appl. Phys. **97**, 023701 (2005).
[27] W. Shockley and W. T. Read, Phys. Rev. **87**, 835 (1952).
[28] J. Batista, A. Mandelis, and D. Shaughnessy, Appl. Phys. Lett. **82**, 4077 (2003).
[29] M. E. Rodriguez, A. Mandelis, G. Pan, L. Nicolaides, J. A. Garcia, and Y. Riopel, J. Electrochem. Soc. **147**, 687 (2000), Table I, and references therein.